

# Monitoring Preferential Flow of Water in Sand Using Thermoacoustics Wave Imaging

Chang Liu<sup>1</sup>, Xu Mao<sup>1</sup>, Chang Wang<sup>1</sup>, Rebecca Liyanage<sup>2</sup>, Juan Heredia Juesas<sup>1,3</sup>, Ruben Juanes<sup>2</sup>, Jose Angel Martinez-Lorenzo<sup>1,3</sup>

<sup>1</sup>Department of Mechanical and Industrial Engineering, Northeastern University, Boston, Massachusetts, 02115

<sup>2</sup>Department of Civil and Environmental Engineering, Massachusetts Institute of Technology, Cambridge, Massachusetts, 02139

<sup>3</sup>Department of Electrical and Computer Engineering, Northeastern University, Boston, Massachusetts, 02115

## Key Points:

- The relationship between water saturation in sand and the resultant thermoacoustics wave amplitude is monotonic.
- The reconstructed thermoacoustics images match well with the optical ground truth for water-saturated sand.
- Thermoacoustics imaging enables real-time monitoring of water distribution in subsurface sand.

---

Corresponding author: Chang Liu, [liu.chang4@northeastern.edu](mailto:liu.chang4@northeastern.edu)

Corresponding author: Jose Angel Martinez-Lorenzo, [j.martinez-lorenzo@northeastern.edu](mailto:j.martinez-lorenzo@northeastern.edu)

**Abstract**

Accurate predictions of fluid flow, mass transport, and reaction rates critically impact the efficiency and reliability of subsurface exploration and sustainable use of subsurface resources. Quantitative dynamical sensing and imaging can play a pivotal role in the ability to make such predictions. Geophysical thermoacoustic technology has the potential to provide the aforementioned capabilities, since it builds upon the principle that electromagnetic and mechanical wave fields can be coupled through a thermodynamic process. In this letter, we present laboratory experiments featuring the efficacy of thermoacoustic imaging in the monitoring of preferential flow of water in porous media. Our laboratory experimental equipment can be readily packaged in a form factor that fits in a borehole, and the use of multiple acoustic transducers—which can be combined with volumetric coding techniques—has the potential to provide quasi-real-time imaging (0.5 Hertz video rate) of regions in close proximity (a few meters) of an open field well.

**Plain Language Summary**

Multiphysics subsurface sensing and imaging technology has the potential to provide unique insights to better understand multiphase flow and transport in porous media in 4D (time and space). Conventional high-resolution, laboratory-based imaging technology—such as X-ray or MRI—require power-hungry and often bulky equipment; the latter limits their use in open field experiments and challenges their ability to perform real-time image reconstruction. Acoustics Doppler imaging has been used for real-time flow velocity monitoring in biomedical applications; however, the relationship between fluid saturation in porous media and measured acoustic pressure still requires further investigation. In this letter we show how microwave-induced thermoacoustic (TA) imaging technology can be applied to monitor water distribution in sand. In contrast to traditional acoustic imaging, the proposed TA method exhibits a dominant monotonic relationship between the degree of water saturation and the measured amplitude of the TA pressure. Our experimental results show the efficacy of TA technology for imaging 2D water distribution profiles in sand. The reconstructed TA images are in good agreement with the optical ground truth water distribution map, thus illustrating the feasibility of the proposed method for real-world field applications in agricultural and hydrological sciences.

**1 Introduction**

Understanding the distribution of fluid phases during multiphase flow in porous media is critical in a wide array of subsurface natural processes and engineering applications (Jarvis, 2007; Blunt et al., 2013; Berg et al., 2013). Optical imaging, X-ray tomography, and magnetic resonance imaging (MRI) are just a few of the most commonly used non-invasive, high-resolution imaging techniques (Katuwal et al., 2018; Pohlmeier et al., 2018; Cnudde & Boone, 2013). However, these methods are subject to important drawbacks that not only limit their use in field applications but also in controlled laboratory environments (Werth et al., 2010; Wildenschild et al., 2002). Optical imaging techniques are well suited to reconstruct fluid distribution in a real-time fashion; however, their use is mostly limited to 2D geometries due reduced penetration on light in highly opaque media and fluid saturation cannot be easily quantified (Moebius & Or, 2012; Roman et al., 2020), although advances such as refraction-index matching, planar laser-induced fluorescence and confocal microscopy have extended the range of application of 3D optical (Kong et al., 2011; Sharma et al., 2011; Krummel et al., 2013; Dalbe & Juanes, 2018). In contrast, X-ray and MRI methods can provide a quantified high-resolution image of 3D geometries (Pohlmeier et al., 2018; Liyanage et al., 2019); however, these methods are limited in their ability to capture the transient behavior of fast fluid flow due to its intrinsic slow scanning speed (Luo et al., 2008; Koestel & Larsbo, 2014). For example, preferential flow, which refers to the phenomenon of channeling in

68 filtrating water as a result of ‘macropores’ (Beven & Germann, 1982) or gravitational  
69 instability (Glass et al., 1989; Wei et al., 2014; Liyanage & Juanes, 2021), can reach a  
70 wetting front velocity up several millimeters per second, calling for a real-time imaging  
71 method in 3D (Zhang et al., 2018; Jarvis et al., 2016; Beven & Germann, 2013).

72 Acoustic (AC) and seismic waves are commonly used for subsurface situational aware-  
73 ness (Müller et al., 2012; David et al., 2015); however, the intrinsic relationship between  
74 acoustic properties of rocks and fluid saturation remains poorly understood. Neverthe-  
75 less, it has been shown that an increase in water saturation modulates the amplitude of  
76 P-waves, which ultimately gives form to the acoustics signature of heterogeneous mix-  
77 tures of rocks and fluids (Pimienta et al., 2019; David et al., 2017). While ultrasound  
78 imaging has been applied in geophysics, the vague relationship between the morphology  
79 of the sample under test and ultrasound image suggests that further advances are needed  
80 before this methodology can be used in quantitative dynamical imaging applications (Zou  
81 et al., 2016, 2018).

82 TA sensing and imaging presents a new opportunity to better characterize the sub-  
83 surface due to its inherent multiphysics nature, in which elastic waves are created due  
84 to the thermal expansion and contraction of a target when it is illuminated by a high  
85 intensity microwave source (Liu et al., 2018). This technology, originally used for breast  
86 cancer detection, leverages on the high contrast existing between healthy and cancerous  
87 tissues at microwaves frequencies and the high resolution of AC technology to create im-  
88 ages with a pixel resolution of tens of micrometers (Lou et al., 2012). Such a thermodynamics-  
89 driven coupling of electromagnetic and mechanical waves overcomes the intrinsic poor  
90 resolution of electromagnetic images and the low contrast of AC images when used in  
91 a standalone fashion (Cui et al., 2017; Xu & Wang, 2006). At particular spatial scales,  
92 there are certain similarities amongst the constitutive properties of biological and geo-  
93 logical materials—suggesting that TA technology may be used for geophysical imaging  
94 applications. The latter assumption was experimentally tested and validated in (Liu et  
95 al., 2019); the authors demonstrated that geological materials, such as sand and rocks,  
96 can indeed generate detectable TA pressure waves. Moreover, the significant contrast ex-  
97 isting between the dielectric constants of water and quartz sand enables the monitoring  
98 of fluid distribution in sandy environments.

99 Conventional real-time imaging systems use arrays of transducers, often involving  
100 over 100 receivers, to collect large amounts of information in a reduced amount of time;  
101 however, these bulky, power-hungry, and often expensive devices constrain the use of TA  
102 imaging in open field scenarios (Yin et al., 2004). TA technology is well poised to en-  
103 able real-time imaging while using a reduced number of receivers. The latter is afforded  
104 by performing volumetric spatial coding of the wave fields (Lorenzo et al., 2015) to max-  
105 imize the sensing capacity of the imaging system, which is defined as the information-  
106 transfer efficiency between imaging domain and the measured data. Volumetric coding  
107 can be performed using artificial metamaterials, holey cavities, and compressive reflec-  
108 tors; this reduces the mutual information among successive measurements and increase  
109 the sensing capacity of the imaging system (Mao et al., 2020).

110 In this letter we present the first study showing the efficacy of microwave-induced  
111 thermoacoustics imaging to monitor fluid distribution in geological media. This technique  
112 has the potential to offer real-time reconstruction of fluid flow in 4D, at distance, and  
113 using non-contact sensors—an ability that could prove instrumental to extend our un-  
114 derstanding of water distribution and heterogeneous infiltration in the Earth’s critical  
115 zone (Richter & Mobley, 2009). This letter is structured as follows: In Section 2 we in-  
116 troduce the background theory of applying TA waves to monitor water distribution in  
117 sand. Based on this, we establish a simulation model to predict the relationship between  
118 water saturation and the TA signal strength. We design an experiment to validate this  
119 principle. In Section 3, we analyze the data from the simulation and experiment, both  
120 showing a monotonic relationship between water saturation and TA signal amplitude.

Table 1: Material properties used in simulation

Material	$\epsilon_r$	$\sigma$ [S/m]	$\rho$ [kg/m <sup>3</sup> ]	$\kappa$ [GPa]	$\beta$ [10 <sup>-6</sup> /K]	$C_p$ [J/(kg·K)]
Quartz Sand	4.27	0	2650	37	1	743
Water	80	0.05	1000	2.25	210	4180
Air	1	0	-	-	-	-
Oil	2.6	0.01	-	-	-	-
Acrylic Sheet	3.4	$6.7 \times 10^{-15}$	-	-	-	-

121 In Section 4 we present the experimental results of recovering the water distribution pro-  
 122 file in a quasi-3D sand cell (in which one dimension is smaller than the other two), and  
 123 in Section 5 we summarize the main outcomes of our study.

## 124 2 Materials and Methods

Microwave induced TA pressure waves are generated due to the thermal expansion of an object when it is illuminated by a short, intense microwave pulse. The governing equations for TA wave are:

$$\nabla^2 p(\mathbf{r}, t) - \frac{1}{c^2(\mathbf{r})} \frac{\partial^2}{\partial t^2} p(\mathbf{r}, t) = - \frac{\beta(\mathbf{r})}{C_p(\mathbf{r})} \frac{\partial Q(\mathbf{r}, t)}{\partial t} \quad (1a)$$

$$Q(\mathbf{r}, t) \approx \sigma(\mathbf{r}) \|E(\mathbf{r})\|^2 f^2(t) \quad (1b)$$

125 where  $p(\mathbf{r}, t)$  is the pressure,  $c(\mathbf{r})$  is the sound speed,  $\beta(\mathbf{r})$  is the thermal expansion rate,  
 126  $C_p(\mathbf{r})$  is the heat capacity, and  $Q(\mathbf{r}, t)$  is the heat source. This term is defined in Eq. (1b),  
 127 where  $\sigma(\mathbf{r})$  is the electric conductivity,  $\mathbf{E}(\mathbf{r})$  is the electric field, and  $f(t)$  is the excita-  
 128 tion pulse function. According to Eq. (1b), the right hand side of Eq. (1a) can be writ-  
 129 ten as  $-\frac{\beta(\mathbf{r})}{C_p(\mathbf{r})} \sigma(\mathbf{r}) \|E(\mathbf{r})\|^2 \frac{\partial}{\partial t} f^2(t)$ . This term can be decomposed as the product of two  
 130 functions: one is a time varying modulating signal  $\frac{\partial}{\partial t} f^2(t)$ ; and the other is a material-  
 131 dependent space varying distribution  $S(\mathbf{r}) = -\frac{\beta(\mathbf{r})}{C_p(\mathbf{r})} \sigma(\mathbf{r}) \|E(\mathbf{r})\|^2$ . The constitutive prop-  
 132 erties within the source term  $S(\mathbf{r})$  are affected by the water saturation of the sandy porous  
 133 medium, and their value can be approximated by empirical rock physics models (RPMs).  
 134 The latter provides an estimation of the constitutive properties of the compound mix-  
 135 ture and the volume fraction of each one of its individual components.

136 Our first experiment is aimed at the computational modeling and experimental test-  
 137 ing of the effect of water saturation on the signal strength. A multiphysics engine (Inc.,  
 138 2020) was used to reveal such relationship. Figure 1a displays the baseline geometry of  
 139 the simulation; the material properties are predicted using the RPMs described in (Shen  
 140 et al., 1985; Troschke & Burkhardt, 1998; Waples & Waples, 2004) and summarized in  
 141 Table 1—where  $\epsilon_r$  is the relative permittivity,  $\rho$  is the density, and  $\kappa$  is the bulk mod-  
 142 ulus. TA pressure signals as well as the source strength predicted by the computational  
 143 models are contrasted with those experimentally measured in the first of our TA imag-  
 144 ing testbeds. Six sand samples having different quantitatively-controlled saturation lev-  
 145 els are prepared for the experiment.

146 The second experiment is aimed at demonstrating that TA imaging can effectively  
 147 be used to monitor fingered water infiltration in a quasi-3D sand cell. The testbed is shown  
 148 in Fig. 1c. Since only one transducer is applied in the experiment, the sand cell with static  
 149 water distribution is imaged.

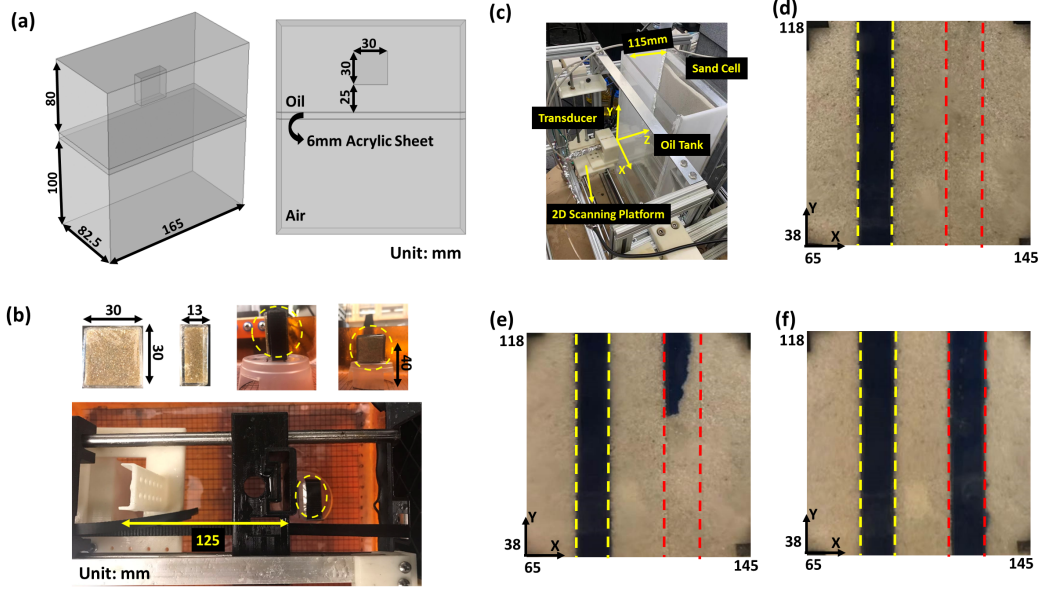


Figure 1: Monitoring water distribution profile in sand using the TA wave: (a) RPM-driven simulation geometry, (b) the testbed for the first experiment, (c) the testbed for the second experiment, (d) water distribution inside the marker, (e) water distribution after the first injection, and (f) water distribution after the second injection.

### 3 Data Collection

In the first experiment, a plastic box with one facet removed is filled with 12.5g of sand (#20 graded). The size of the sand box is 30mm×30mm×13mm, as shown in Fig. 1b. While keeping the dry sample for comparison, the other five samples are injected with different amounts of water: 0.7g, 1.4g, 2.1g, 2.8g, and 3.5g, separately. Provided that the porosity of sand sample is  $\Phi = 30\%$ , this results in water saturations of 20%, 40%, 60%, 80%, and 100% for each sample, respectively. Later, the sand box is sealed with a thin layer of plastic wrap and black waterproof tape. Finally, the sand box is held still for 1 hour to allow for the water to spread through the sample, since the water is injected from the opening facet of the sample. As it can be seen in Fig. 1b, the sand sample is placed parallel to the transducer in the oil bath at a distance of 125mm away from the transducer. Moreover, the center of the sand sample is lifted 40mm to match the height of the transducer. After one measurement is finished, the previous sand box is replaced with another sand sample with different saturation level.

In the second experiment, the quasi-3D sand cell (10mm thickness) is separated from the acoustic transducer by an oil tank. The distance between the sand cell and the transducer is 115mm. The sand sample under test is geometrically constrained to a small narrow region using a plastic enclosure, and two such enclosures are prepared: the left one is fully saturated as the marker for reference (yellow dashed line in Fig. 1d), and the right one is for dynamic water distribution imaging (red dashed line in Fig. 1d). In the first part of this experiment, 1.5mL of blue-dyed water is injected from the top into the right enclosure, which is shown in Fig. 1e. In the second part of this experiment, additional amount of 3.9mL of blue-dyed water is injected into the right enclosure, and the final water distribution is shown in Fig. 1f. In this experiment, the selected imaging area ranges from  $X = 65\text{mm}$  to  $X = 145\text{mm}$ ,  $Y = 38\text{mm}$  to  $Y = 118\text{mm}$ , and  $Z = 100\text{mm}$  to  $Z = 140\text{mm}$ . The scanning range of transducer is slightly larger than the imaging area to achieve

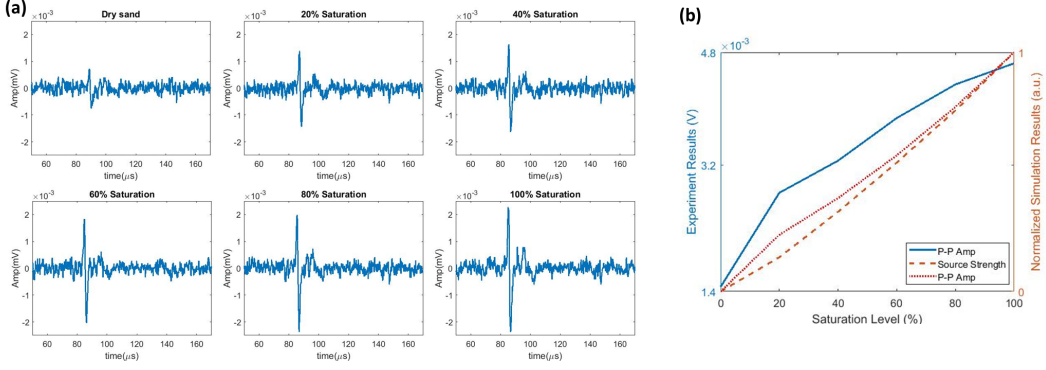


Figure 2: The monotonic relationship between water saturation and the TA amplitude: (a) measured signals of the sand box saturated by different amount of water, and (b) the peak-peak amplitude of the collected signals (solid line), the simulated source strength (dashed line) and the peak-peak amplitude (dotted line) after normalization.

176 better resolution in X-Y plane, ranging from  $X = 53\text{mm}$  to  $X = 157\text{mm}$  in X-direction  
 177 and  $Y = 26\text{mm}$  to  $Y = 130\text{mm}$  in Y-direction. The raster scan is conducted four times:  
 178 dry sand, after the preparation of the marker, after the first injection and after the second  
 179 injection into the right enclosure. Moreover, to guarantee the fully spread of water,  
 180 the raster scan starts after the water profile stops moving. The measurements are collected  
 181 with 4mm spatial separation for every measured point, thus making a total number  
 182 of 729 measurements for each scan. During these scans, the power of the EM wave  
 183 remains constant, and the difference between the successive measurements should be the  
 184 effect of the injected water.

185 **4 Results**

186 In the first experiment, the collected TA signals for samples with different water  
 187 saturations are plotted in Fig. 2a. As it can be seen, the amplitudes of the measured sig-  
 188 nals depend on the amount of water in the sand. The peak-peak value of those signals  
 189 are plotted in Fig. 2b, and the simulated source strengths as well as the peak-peak am-  
 190 plitudes are also shown for comparison after normalization. Several points in Fig. 2b  
 191 deserve discussion. All results in Fig. 2b exhibit a strictly monotonic relationship between  
 192 the TA signal amplitude with the amount of injected water, which reveals the feasibil-  
 193 ity of distinguishing the water saturation in sand using TA waves. The simulated results  
 194 of peak-peak amplitude and source strength both show a nearly linear relationship against  
 195 the saturation level, which can be used as a prediction for the water saturation level in  
 196 the following experiment. We also observe that the dry sand can transmit a detectable  
 197 TA wave in the experiment while the simulation result shows a zero source strength. This  
 198 is because the sand used in the experiment is not fully dehydrated. Furthermore, the trend  
 199 of the experimental measurements exhibit a reversed curvature when compared to that  
 200 of the simulated results, which may be attributed to by several factors. Firstly, the nu-  
 201 merical simulation considers the sample to have a homogeneous distribution of water sat-  
 202 uration; while the experiment may have a heterogeneous one due to the water injection  
 203 in the open facet of the box. Secondly, there may exist important differences between  
 204 the material properties predicted by the selected RPM and the sand sample used in the  
 205 experiment.

206 In the second experiment, the left enclosure, as shown in Fig. 1d, is fully saturated to  
 207 determine the saturation level of the dynamic water distribution inside the right en-

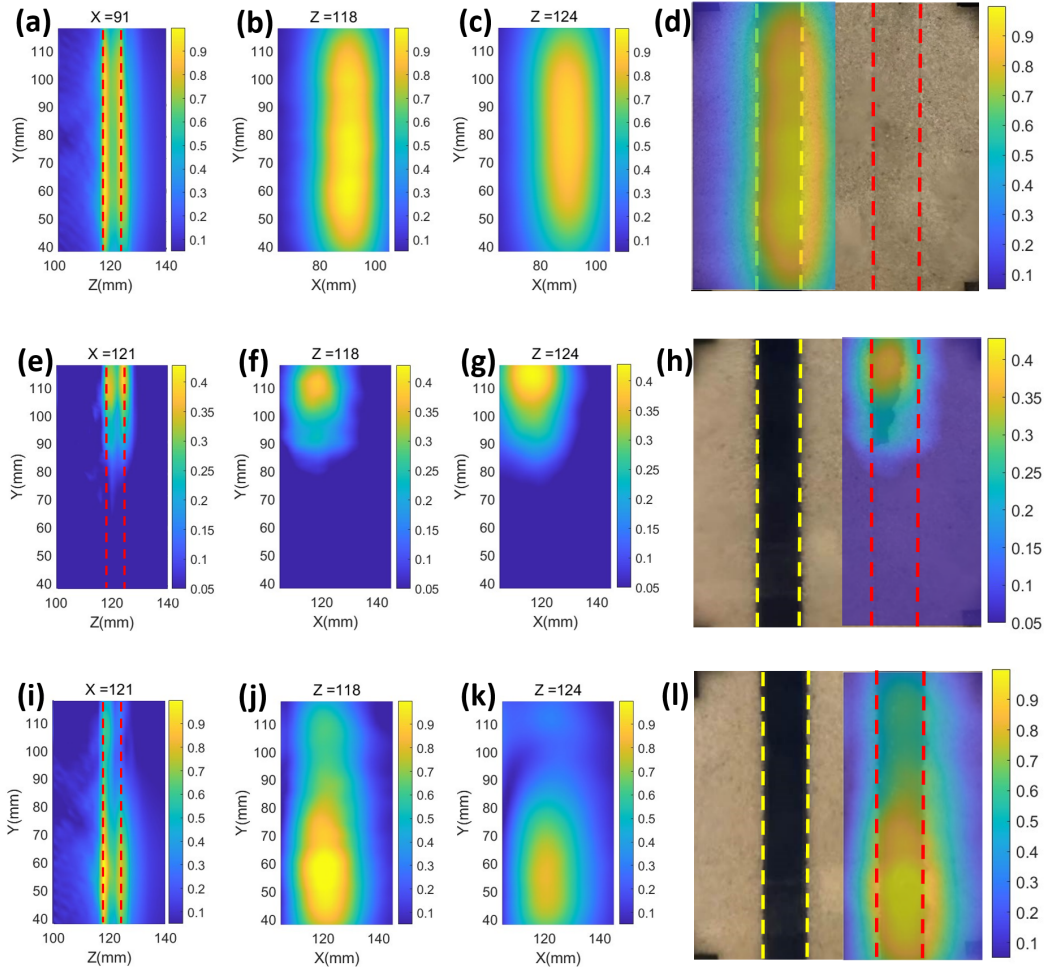


Figure 3: Water distribution reconstruction using the TA waves: (a) slice taken at  $X = 91$ mm for marker, (b) slice taken at  $Z = 118$ mm for marker, (c) slice taken at  $Z = 124$ mm for marker, (d) overlapping marker image with ground truth, (e) slice taken at  $X = 121$ mm for the first injection, (f) slice taken at  $Z = 118$ mm for the first injection, (g) slice taken at  $Z = 124$ mm for the first injection, (h) overlapping the first injection image with ground truth, (i) slice taken at  $X = 121$ mm for the second injection, (j) slice taken at  $Z = 118$ mm for the second injection, (k) slice taken at  $Z = 124$ mm for the second injection, and (l) overlapping the second injection image with ground truth.

208 closure based on the simulated results presented in the first experiment. The images af-  
 209 ter first infiltration—Fig. 1e—show that the color intensity of the fluid map is mainly  
 210 remained on the top. Moreover, the fluid distribution after the second injection has spread  
 211 to the whole area of the enclosure compared with the first injection. This visual infor-  
 212 mation is used as optical ground truth to drive the comparison with the TA image.

213 Figure 3a presents the imaging result of a cross section ( $X = 91\text{mm}$ ) for the marker  
 214 area, which shows the capability of TA imaging to recover subsurface information of the  
 215 sandy medium. It is noteworthy that the position of the selected cross section is not at  
 216 the center of the imaging area but, rather, at the center of the marker area. As shown  
 217 in Fig. 3a, the intensity of the image stays constant from top to the bottom of the en-  
 218 closure, in agreement with the optical ground truth of Fig. 1d. Furthermore, the first  
 219 peak appears at  $Z = 118\text{mm}$  and the second peak appears at  $Z = 124\text{mm}$  in the image,  
 220 corresponding to the front and back boundary of the sand cell, individually. In addition,  
 221 the image strength at the first and second peaks is similar because the EM wave is trans-  
 222 mitted from the back (negative  $X$  direction), which partly compensates for the atten-  
 223 uation effect. The reconstructed images of the water infiltration profile in the  $X$ - $Y$  plane  
 224 are shown in Figs. 3b and 3c, which correspond to the slice taken at  $Z = 118\text{mm}$  and  
 225  $Z = 124\text{mm}$ , respectively. Both recovered images show an uniform distribution inside  
 226 the area of the enclosure. Figure 3d overlaps the ground truth of marker with the front  
 227 boundary image. Figures 3e-h present the imaging results after the first injection. In con-  
 228 trast with Fig. 3a, the image strength in Fig. 3e stays on the top part of the enclosure,  
 229 which agrees with the ground truth in Fig. 3h. Compared with those results of the first  
 230 injection, the recovered images for the second injection in Figs. 3i-l show an increased  
 231 concentration in the bottom part of the enclosure. It is also noticed that Figs. 3j and  
 232 3k slightly differ from each other because the water distribution is not uniform in the  
 233 thickness direction.

234 Additionally, it is also observed that there exists about 3mm difference between  
 235 the ground truth and the image in  $Z$ -direction as shown in Fig. 3a, which is due to the  
 236 device delay. In addition, Figs. 3e and 3i also recover the front and back boundaries at  
 237  $Z = 118\text{mm}$  and  $Z = 124\text{mm}$ , which proves that 3mm's delay is constant for different  
 238 scans. Furthermore, the distance between two boundaries is just 6mm, smaller than thick-  
 239 ness of the sand cell. There are two factors contributing to this result: firstly, the acous-  
 240 tics properties of water-saturated sand are assumed to be unknown during the image re-  
 241 construction, and the properties of oil are used instead; secondly, the thickness of marker  
 242 enclosure is smaller than the thickness of sand cell, which is about 6.5mm. Despite these  
 243 precision tolerances, our TA imaging accurately recovers the shape of the water distri-  
 244 bution in the testbed.

## 245 5 Conclusions

246 In this letter, we have demonstrated that thermoacoustic pressure waves, which re-  
 247 sult from the thermodynamic coupling of electromagnetic and mechanical waves, can be  
 248 used for detecting and discerning water saturation in the subsurface. Moreover, the re-  
 249 lationship between the amplitude of the thermoacoustic pressure wave and the water sat-  
 250 uration level is strictly monotonic, as predicted by our computational simulation and val-  
 251 idated by the experimental data. On the basis of this result, we conducted a second ex-  
 252 periment that demonstrated the feasibility of using thermoacoustic waves to reconstruct  
 253 fluid distribution in a quasi-3D sand cell. The superficial water saturation levels inferred  
 254 from the optical ground truth images are in good agreement with the images reconstructed  
 255 with our thermoacoustic data. Both optical and thermoacoustic images reveal the intrin-  
 256 sic effect of gravity on the distribution of the fluid on the porous media; however ther-  
 257 moacoustic imaging have the ability to do so quantitatively and in 3D. For the sake of  
 258 reliability and simplicity in this first demonstration, only one mechanically scanned trans-  
 259 ducer was used to collect the TA data; a choice that limits the scanning speed and does

260 not have the temporal resolution necessary to track the dynamic gravity-driven fluid mo-  
 261 tion. Ongoing efforts in our lab are currently geared towards performing real-time imag-  
 262 ing of fluid flow in porous media by using arrays of receiving transducers and volumet-  
 263 ric coding fused with compressive imaging.

## 264 Open Research

265 The imaging algorithm is introduced in the supplementary file, and the experiment  
 266 data is available on the Zenodo platform via <https://doi.org/10.5281/zenodo.7465796>.

## 267 Acknowledgments

268 This work has been partially funded by the Department of Energy (Award DE-SC0017614)  
 269 and the NSF CAREER program (Award No. 1653671). RL was partly supported by the  
 270 Abdul Latif Jameel World Water and Food Security Lab (J-WAFS) at MIT. RJ acknowl-  
 271 edges funding from the US Department of Energy (Award DE-SC0018357).

## 272 References

- 273 Berg, S., Ott, H., Klapp, S. A., Schwing, A., Neiteler, R., Brussee, N., . . . others  
 274 (2013). Real-time 3D imaging of Haines jumps in porous media flow. *Proceed-*  
 275 *ings of the National Academy of Sciences*, 110(10), 3755–3759.
- 276 Beven, K., & Germann, P. (1982). Macropores and water flow in soils. *Water Re-*  
 277 *sour. Res.*, 18(5), 1311–1325.
- 278 Beven, K., & Germann, P. (2013). Macropores and water flow in soils revisited. *Wa-*  
 279 *ter Resources Research*, 49(6), 3071–3092.
- 280 Blunt, M. J., Bijeljic, B., Dong, H., Gharbi, O., Iglauer, S., Mostaghimi, P., . . .  
 281 Pentland, C. (2013). Pore-scale imaging and modelling. *Advances in Water*  
 282 *resources*, 51, 197–216.
- 283 Cnudde, V., & Boone, M. N. (2013). High-resolution x-ray computed tomography  
 284 in geosciences: A review of the current technology and applications. *Earth-*  
 285 *Science Reviews*, 123, 1–17.
- 286 Cui, Y., Yuan, C., & Ji, Z. (2017). A review of microwave-induced thermoacoustic  
 287 imaging: Excitation source, data acquisition system and biomedical applica-  
 288 tions. *Journal of Innovative Optical Health Sciences*, 10(04), 1730007.
- 289 Dalbe, M. J., & Juanes, R. (2018). Morphodynamics of fluid–fluid displacement in  
 290 3d deformable granular media. *Phys. Rev. Applied*, 9, 024028.
- 291 David, C., Barnes, C., Desrues, M., Pimienta, L., Sarout, J., & Dautriat, J. (2017).  
 292 Ultrasonic monitoring of spontaneous imbibition experiments: Acoustic signa-  
 293 ture of fluid migration. *Journal of Geophysical Research: Solid Earth*, 122(7),  
 294 4931–4947.
- 295 David, C., Bertauld, D., Dautriat, J., Sarout, J., Menéndez, B., & Nabawy, B.  
 296 (2015). Detection of moving capillary front in porous rocks using x-ray and  
 297 ultrasonic methods. *Frontiers in Physics*, 3, 53.
- 298 Glass, R. J., Parlange, J.-Y., & Steenhuis, T. S. (1989). Wetting front instability, 2.  
 299 Experimental determination of relationships between system parameters and  
 300 two-dimensional unstable flow field behaviour in initially dry porous media.  
 301 *Water Resour. Res.*, 25(6), 1195–1207.
- 302 Heredia-Juesas, J., Molaei, A., Tirado, L., & Martínez-Lorenzo, J. Á. (2021). Con-  
 303 sensus and sectioning-based adm with norm-1 regularization for imaging  
 304 with a compressive reflector antenna. *IEEE Transactions on Computational*  
 305 *Imaging*, 7, 1189–1204.
- 306 Inc., C. (2020). *Comsol* [software]. v5.2. Retrieved from [http://www.comsol.com/](http://www.comsol.com/products/multiphysics/)  
 307 [products/multiphysics/](http://www.comsol.com/products/multiphysics/)

- 308 Jarvis, N. (2007). A review of non-equilibrium water flow and solute transport  
 309 in soil macropores: Principles, controlling factors and consequences for water  
 310 quality. *European Journal of Soil Science*, *58*(3), 523–546.
- 311 Jarvis, N., Koestel, J., & Larsbo, M. (2016). Understanding preferential flow in  
 312 the vadose zone: Recent advances and future prospects. *Vadose Zone Journal*,  
 313 *15*(12), 1–11.
- 314 Katuwal, S., Hermansen, C., Knadel, M., Moldrup, P., Greve, M. H., & de Jonge,  
 315 L. (2018). Combining x-ray computed tomography and visible near-infrared  
 316 spectroscopy for prediction of soil structural properties. *Vadose Zone Journal*,  
 317 *17*(1), 160054.
- 318 Koestel, J., & Larsbo, M. (2014). Imaging and quantification of preferential solute  
 319 transport in soil macropores. *Water Resources Research*, *50*(5), 4357–4378.
- 320 Kong, X.-Z., Holzner, M., Stauffer, F., & Kinzelbach, W. (2011). Time-resolved  
 321 3D visualization of air injection in a liquid-saturated refractive-index-matched  
 322 porous medium. *Exp. Fluids*, *50*(6), 1659–1670.
- 323 Krummel, A. T., Datta, S. S., Münster, S., & Weitz, D. A. (2013). Visualizing  
 324 multiphase flow and trapped fluid configurations in a model three-dimensional  
 325 porous medium. *AIChE J.*, *59*(3), 1022–1029.
- 326 Liu, C., Ghanbarzadeh-Dagheyani, A., Heredia-Juesas, J., Molaei, A., & Martinez-  
 327 Lorenzo, J. A. (2018). The study of holey cavity in the application of thermoacoustics  
 328 imaging. In *ASME International Mechanical Engineering Congress and Exposition* (Vol. 52163,  
 329 p. V011T01A025).
- 330 Liu, C., Mao, X., Heredia Juesas, J., Molaei, A., & Martinez-Lorenzo, J. A. (2019).  
 331 Preliminary results of microwave induced thermoacoustics imaging in geological  
 332 media. In *ASME International Mechanical Engineering Congress and Exposition* (Vol. 59483,  
 333 p. V011T01A017).
- 334 Liyanage, R., Cen, J., Krevor, S., Crawshaw, J. P., & Pini, R. (2019). Multidimen-  
 335 sional observations of dissolution-driven convection in simple porous media  
 336 using x-ray ct scanning. *Transp. Porous Media*, *126*(2), 355–378.
- 337 Liyanage, R., & Juanes, R. (2021). *Electronic data repository for ‘Gravity finger-  
 338 ing control on evaporation and deep drainage in a 3D porous medium’*. URL:  
 339 <https://doi.org/10.5281/zenodo.4425884>.
- 340 Lorenzo, J. A. M., Juesas, J. H., & Blackwell, W. (2015). A single-transceiver com-  
 341 pressive reflector antenna for high-sensing-capacity imaging. *IEEE Antennas  
 342 and Wireless Propagation Letters*, *15*, 968–971.
- 343 Lou, C., Yang, S., Ji, Z., Chen, Q., & Xing, D. (2012). Ultrashort microwave-  
 344 induced thermoacoustic imaging: a breakthrough in excitation efficiency and  
 345 spatial resolution. *Physical review letters*, *109*(21), 218101.
- 346 Luo, L., Lin, H., & Halleck, P. (2008). Quantifying soil structure and preferen-  
 347 tial flow in intact soil using x-ray computed tomography. *Soil Science Society  
 348 of America Journal*, *72*(4), 1058–1069.
- 349 Mao, X., Liu, C., Heredia-Juesas, J., & Martinez-Lorenzo, J. A. (2020). Microwave-  
 350 induced thermoacoustic compressive imaging with metamaterial coding. In  
 351 *Asme international mechanical engineering congress and exposition* (Vol.  
 352 84478, p. V001T01A018).
- 353 Moebius, F., & Or, D. (2012). Interfacial jumps and pressure bursts during fluid dis-  
 354 placement in interacting irregular capillaries. *Journal of colloid and interface  
 355 science*, *377*(1), 406–415.
- 356 Müller, S., Niederleithinger, E., & Bohlen, T. (2012). Reverse time migration: A  
 357 seismic imaging technique applied to synthetic ultrasonic data. *International  
 358 Journal of Geophysics*, *2012*, 128465.
- 359 Pimienta, L., David, C., Sarout, J., Perrot, X., Dautriat, J., & Barnes, C. (2019).  
 360 Evolution in seismic properties during low and intermediate water satura-  
 361 tion: Competing mechanisms during water imbibition? *Geophysical Research  
 362 Letters*, *46*(9), 4581–4590.

- 363 Pohlmeier, A., Garré, S., & Roose, T. (2018). Noninvasive imaging of processes in  
 364 natural porous media: From pore to field scale. *Vadose zone journal*, *17*(1), 1–  
 365 3.
- 366 Richter, D. d., & Mobley, M. L. (2009). Monitoring Earth’s critical zone. *Science*,  
 367 *326*, 1067–1068.
- 368 Roman, S., Soulaire, C., & Kavscek, A. R. (2020). Pore-scale visualization and char-  
 369 acterization of viscous dissipation in porous media. *Journal of Colloid and In-*  
 370 *terface Science*, *558*, 269–279.
- 371 Sharma, P., Aswathi, P., Sane, A., Ghosh, S., & Bhattacharya, S. (2011). Three-  
 372 dimensional real-time imaging of bi-phasic flow through porous media. *Rev.*  
 373 *Sci. Instrum.*, *82*, 113704.
- 374 Shen, L., Savre, W., Price, J., & Athavale, K. (1985). Dielectric properties of reser-  
 375 voir rocks at ultra-high frequencies. *Geophysics*, *50*(4), 692–704.
- 376 Troschke, B., & Burkhardt, H. (1998). Thermal conductivity models for two-phase  
 377 systems. *Physics and Chemistry of the Earth*, *23*(3), 351–355.
- 378 Waples, D. W., & Waples, J. S. (2004). A review and evaluation of specific heat  
 379 capacities of rocks, minerals, and subsurface fluids. part 1: Minerals and non-  
 380 porous rocks. *Natural resources research*, *13*(2), 97–122.
- 381 Wei, Y., Cejas, C. M., Barrois, R., Dreyfus, R., & Durian, D. J. (2014). Morphology  
 382 of rain water channeling in systematically varied model sandy soils. *Phys. Rev.*  
 383 *Applied*, *2*, 044004.
- 384 Werth, C. J., Zhang, C., Brusseau, M. L., Oostrom, M., & Baumann, T. (2010).  
 385 A review of non-invasive imaging methods and applications in contaminant  
 386 hydrogeology research. *Journal of Contaminant Hydrology*, *113*(1-4), 1–24.
- 387 Wildenschild, D., Vaz, C., Rivers, M., Rikard, D., & Christensen, B. (2002). Using  
 388 x-ray computed tomography in hydrology: systems, resolutions, and limita-  
 389 tions. *Journal of Hydrology*, *267*(3-4), 285–297.
- 390 Xu, M., & Wang, L. V. (2006). Photoacoustic imaging in biomedicine. *Review of sci-*  
 391 *entific instruments*, *77*(4), 041101.
- 392 Yin, B., Xing, D., Wang, Y., Zeng, Y., Tan, Y., & Chen, Q. (2004). Fast photoa-  
 393 coustic imaging system based on 320-element linear transducer array. *Physics*  
 394 *in Medicine & Biology*, *49*(7), 1339.
- 395 Zhang, Y., Zhang, Z., Ma, Z., Chen, J., Akbar, J., Zhang, S., . . . Cerdà, A. (2018).  
 396 A review of preferential water flow in soil science. *Canadian Journal of Soil*  
 397 *Science*, *98*(4), 604–618.
- 398 Zou, X., Song, H., Wang, C., & Ma, Z. (2016). Relationships between b-mode ultra-  
 399 sound imaging signals and suspended sediment concentrations. *Measurement*,  
 400 *92*, 34–41.
- 401 Zou, X., Wang, C., Song, H., Han, Z., Ma, Z., & Hu, W. (2018). Applications  
 402 of ultrasound imaging system for measuring water-sand parameters during  
 403 sediment transport process in hydraulic model experiments. *Journal of Hy-*  
 404 *droinformatics*, *20*(2), 410–423.